

all of the H- and L-chain mutations required for bnAb activity against the native CD4bs. Indeed, no neutralizing activity was detected for any of the 8 eOD-GT8 60mer-induced Abs [all with high affinity ($K_D < 1$ nM) for eOD-GT8 and low affinity ($1 \mu\text{M} < K_D < 100 \mu\text{M}$) for core-e2CC HxB2 N276D] that we tested against a panel of four viruses from clades A and B that included both WT and N276A mutant viruses with increased sensitivity to VRC01-class bnAbs (fig. S18). One design feature of eOD-GT8 is that it lacks the N276 glycan; removal of this glycan is a requirement for germline reactivity (17, 21). However, the N276 glycosylation site is conserved in 94.5% of HIV strains, according to an analysis of 3796 sequences from the Los Alamos HIV database (www.hiv.lanl.gov/). Induction of broad neutralization will probably require one or more boosting immunogens bearing a glycan at N276 so as to select mutations to accommodate that glycan (17). On the H chain of VRC01-class bnAbs, mutations in the CDR2, CDR1, FW1, and FW3 are likely required for maximum potency and breadth (24, 40), and native-like Env immunogens will probably be needed to select for these. In sum, boosting with a sequence of increasingly native-like antigens, and potentially including cocktails of different antigens within each boost to mimic the antigenic diversity of the CD4bs, will likely be needed to select the mutations required for VRC01-class bnAb activity. The mouse model presented here, as well as other newly developed VRC01-class knock-in mouse models (41), should aid us to test this notion and can be used to identify the antigens and boosting strategies that work best. Of note, we demonstrated here that a single immunization with the eOD-GT8 60mer induces VRC01-class antibodies with modest affinity for the core-e2CC HxB2 N276D monomer and 60mer; so these molecules represent promising candidates for the first boost. We are thus mapping the first steps in a sequential strategy for the rational induction of bnAbs against HIV.

REFERENCES AND NOTES

1. H. X. Liao et al., *Nature* **496**, 469–476 (2013).
2. N. A. Doria-Rose et al., *Nature* **509**, 55–62 (2014).
3. M. C. Gaubert et al., *Nat. Med.* **3**, 1389–1393 (1997).
4. J. R. Mascola et al., *Nat. Med.* **6**, 207–210 (2000).
5. P. W. Parren et al., *J. Virol.* **75**, 8340–8347 (2001).
6. B. Moldt et al., *Proc. Natl. Acad. Sci. U.S.A.* **109**, 18921–18925 (2012).
7. J. Pietzsch et al., *Proc. Natl. Acad. Sci. U.S.A.* **109**, 15859–15864 (2012).
8. M. Shingai et al., *J. Exp. Med.* **211**, 2061–2074 (2014).
9. X. Wu et al., *Science* **329**, 856–861 (2010).
10. T. Zhou et al., *Science* **329**, 811–817 (2010).
11. X. Wu et al., *Science* **333**, 1593–1602 (2011).
12. J. F. Scheid et al., *Science* **333**, 1633–1637 (2011).
13. M. Bonsignori et al., *J. Virol.* **86**, 4688–4692 (2012).
14. T. Zhou et al., *Immunity* **39**, 245–258 (2013).
15. I. S. Georgiev et al., *Science* **340**, 751–756 (2013).
16. A. P. West Jr., R. Diskin, M. C. Nussenzweig, P. J. Bjorkman, *Proc. Natl. Acad. Sci. U.S.A.* **109**, E2083–E2090 (2012).
17. J. Jardine et al., *Science* **340**, 711–716 (2013).
18. R. Arnaout et al., *PLOS ONE* **6**, e22365 (2011).
19. B. J. DeKosky et al., *Nat. Med.* **21**, 86–91 (2015).
20. S. Hoot et al., *PLOS Pathog.* **9**, e1003106 (2013).

21. A. T. McGuire et al., *J. Exp. Med.* **210**, 655–663 (2013).
22. X. Xiao et al., *Biochem. Biophys. Res. Commun.* **390**, 404–409 (2009).
23. Single-letter abbreviations for the amino acid residues are as follows: A, Ala; C, Cys; D, Asp; E, Glu; F, Phe; G, Gly; H, His; I, Ile; K, Lys; L, Leu; M, Met; N, Asn; P, Pro; Q, Gln; R, Arg; S, Ser; T, Thr; V, Val; W, Trp; and Y, Tyr.
24. J. R. Mascola, B. F. Haynes, *Immunol. Rev.* **254**, 225–244 (2013).
25. I. S. Georgiev et al., *J. Immunol.* **192**, 1100–1106 (2014).
26. D. Sok et al., *PLOS Pathog.* **9**, e1003754 (2013).
27. X. Xiao, W. Chen, Y. Feng, D. S. Dimitrov, *Viruses* **1**, 802–817 (2009).
28. D. S. Dimitrov, *mAbs* **2**, 347–356 (2010).
29. B. F. Haynes, G. Kelsoe, S. C. Harrison, T. B. Kepler, *Nat. Biotechnol.* **30**, 423–433 (2012).
30. F. Klein et al., *Science* **341**, 1199–1204 (2013).
31. X. Wu et al., *Cell* **161**, 470–485 (2015).
32. M. M. Souto-Carneiro, N. S. Longo, D. E. Russ, H. W. Sun, P. E. Lipsky, *J. Immunol.* **172**, 6790–6802 (2004).
33. A. B. Morelli et al., *J. Med. Microbiol.* **61**, 935–943 (2012).
34. R. W. Sanders et al., *PLOS Pathog.* **9**, e1003618 (2013).
35. J. P. Julien et al., *Science* **342**, 1477–1483 (2013).
36. D. Lyumkis et al., *Science* **342**, 1484–1490 (2013).
37. M. Pancera et al., *Nature* **514**, 455–461 (2014).
38. B. Dey et al., *PLOS Pathog.* **5**, e1000445 (2009).
39. R. Diskin et al., *Science* **334**, 1289–1293 (2011).

40. F. Klein et al., *Cell* **153**, 126–138 (2013).
41. P. Dosenovic et al., *Cell* **161**, 1505–1515 (2015).

ACKNOWLEDGMENTS

We thank T. R. Blane, S. Kupriyanov, and G. S. Martin for technical assistance. The data presented in this manuscript are tabulated in the main paper and in the supplementary materials. This work was supported by the IAVI Neutralizing Antibody Consortium and Center (W.R.S. and D.R.B.); the Collaboration for AIDS Vaccine Discovery funding for the IAVI NAC (W.R.S. and D.R.B.); the Ragon Institute of MGH, MIT and Harvard (D.R.B. and W.R.S.); the Helen Hay Whitney Foundation (J.G.J.); and National Institute of Allergy and Infectious Diseases grants R01-AI073148 (D.N.), P01AI081625 (W.R.S.), and CHAVI-ID 1UM1AI100663 (W.R.S. and D.R.B.). IAVI and the Scripps Research Institute are filing a patent relating to the eOD-GT8 immunogens in this manuscript, with inventors J.G.J., D.W.K., S.M., and W.R.S. Materials and information will be provided under a material transfer agreement.

SUPPLEMENTARY MATERIALS

www.sciencemag.org/content/349/6244/156/suppl/DC1
Materials and Methods
Figs. S1 to S18
Tables S1 to S8
References (42–53)

16 May 2015; accepted 11 June 2015
Published online 18 June 2015;
10.1126/science.aac5894

REPORTS

SOFT ROBOTICS

A 3D-printed, functionally graded soft robot powered by combustion

Nicholas W. Bartlett,^{1,2*} Michael T. Tolley,^{3†} Johannes T. B. Overvelde,¹ James C. Weaver,² Bobak Mosadegh,⁴ Katia Bertoldi,¹ George M. Whitesides,^{2,5} Robert J. Wood^{1,2}

Robotists have begun to design biologically inspired robots with soft or partially soft bodies, which have the potential to be more robust and adaptable, and safer for human interaction, than traditional rigid robots. However, key challenges in the design and manufacture of soft robots include the complex fabrication processes and the interfacing of soft and rigid components. We used multimaterial three-dimensional (3D) printing to manufacture a combustion-powered robot whose body transitions from a rigid core to a soft exterior. This stiffness gradient, spanning three orders of magnitude in modulus, enables reliable interfacing between rigid driving components (controller, battery, etc.) and the primarily soft body, and also enhances performance. Powered by the combustion of butane and oxygen, this robot is able to perform untethered jumping.

Robots are typically composed of rigid components to promote high precision and controllability. Frequently constructed from hard metals such as aluminum and steel, these robots require large machining equipment and an intricate assembly process. In contrast, recent work has explored the possibility of creating soft-bodied robots (1–6) inspired by invertebrates such as cephalopods (7–9) and insect larvae (10), as well as vertebrates, including snakes (11) and fish (12). The use of compliant materials facilitates the development of biologically inspired robotic systems (13) that

are more adaptable (14), safer (15, 16), and more resilient (17) than their fully rigid counterparts.

The design and fabrication of soft robotic systems, however, present significant engineering challenges (18, 19). The bodies of soft robots are typically fabricated in custom-designed molds and require multiple assembly steps (20) or lost-wax techniques (21) to embed actuation. The molds used to create these soft robots are complex and time-consuming to make, especially for prototype designs that are fabricated in small numbers and are constantly evolving. Additionally, some applications (such as ones

requiring untethered robots) require rigid components to power and control the soft body (11, 12, 17) or to perform specific tasks. The interfaces between these rigid components and the soft body of the robot are points of recurring failure.

In nature, many animals employ stiffness gradients to join rigid materials and soft structures while minimizing stress concentrations that could lead to failures at rigid/soft interfaces (22, 23). One of the reasons biological systems often outperform engineered systems is that in nature, which employs self-organization for fabrication, added structural complexity comes at a minimal cost. Emerging digital fabrication technologies (such as 3D printing) are beginning to allow designers to move toward this level of structural complexity, albeit at a larger scale and with fewer materials. These technologies can be used to manufacture geometrically intricate designs as efficiently as simple designs with an equivalent amount of material.

¹School of Engineering and Applied Sciences, Harvard University, Cambridge, MA 02138, USA. ²Wyss Institute for Biologically Inspired Engineering, Harvard University, Cambridge, MA 02138, USA. ³Department of Mechanical and Aerospace Engineering, University of California, San Diego, La Jolla, CA 92093, USA. ⁴Dalio Institute of Cardiovascular Imaging, Department of Radiology, New York–Presbyterian Hospital and Weill Cornell Medical College, New York, NY 10021, USA. ⁵Department of Chemistry and Chemical Biology, Harvard University, Cambridge, MA 02138, USA. *Corresponding author. E-mail: nbartlett@seas.harvard.edu †These authors contributed equally to this work.

We used a multimaterial 3D printer (Connex500, Stratasys) to directly print the functional body of a robot that employs soft material components for actuation, obviating the need for complex molding techniques or assembly (24). The robot body is composed primarily of two nested hemispheroids. The flexible bottom hemispheroid features a small depression that provides an initial volume into which oxygen and butane are injected. Ignition of the gases causes a volumetric expansion (25, 26), launching the robot into the air (Fig. 1, A and B). The top hemispheroid has a modulus of elasticity that ranges over three orders of magnitude (from approximately 1 MPa to 1 GPa) through a stepwise gradient of nine different layers, creating a structure that transitions from highly flexible (rubber-like) to fully rigid (thermoplastic-like). In addition to providing a mechanical interface for the rigid control components, the rigid portion of the top hemispheroid also prevents undesired expansion locally and focuses the energy of combustion into the ground, enhancing the jumping efficiency. Pneumatic legs, which use a nested hemi-ellipsoid design similar to that of the main body, surround the central explosive actuator and are used to tilt the body before a jump, controlling the direction of locomotion. This separation of power and control actuators simplifies actuation and gives greater control over direction.

In order to simplify prototyping, we chose a modular design with a rigid core module containing the control components (which are ex-

pensive and change infrequently during design iteration of the body), connected through a predefined interface to the body of the robot (Fig. 1C). This modularity enables efficient iteration of the robot body design, as well as rapid replacement in the case of destructive testing. The core module contains a custom circuit board, high-voltage power source, battery, miniature air compressor, butane fuel cell, bank of six solenoid valves, oxygen cartridge, pressure regulator, and an internal network of channels to facilitate interfacing between the components as necessary (fig. S1, A and B). The core module is mechanically attached to the rigid portion of the body with a layer of high-strength mushroom-head fasteners. Otherwise, it interfaces with the body only through four tubes (three pneumatic tubes for the legs and one tube for fuel delivery to the combustion chamber) and two wires (which produce the spark in the combustion chamber).

Characterization of nine 3D-printed materials with a set of mechanical tests informed the design of the 3D-printed rigid/soft robot. We performed qualitative twisting experiments to gain an intuitive understanding of the response of the various materials (Fig. 2A). Mechanical testing on a universal testing machine (Instron 5544, Instron) yielded quantitative values of material properties (supplementary text). This information was used to simulate the operation of the robot using finite element analysis (FEA) software, which allowed us to compare the relative efficiency of jumping robots with different

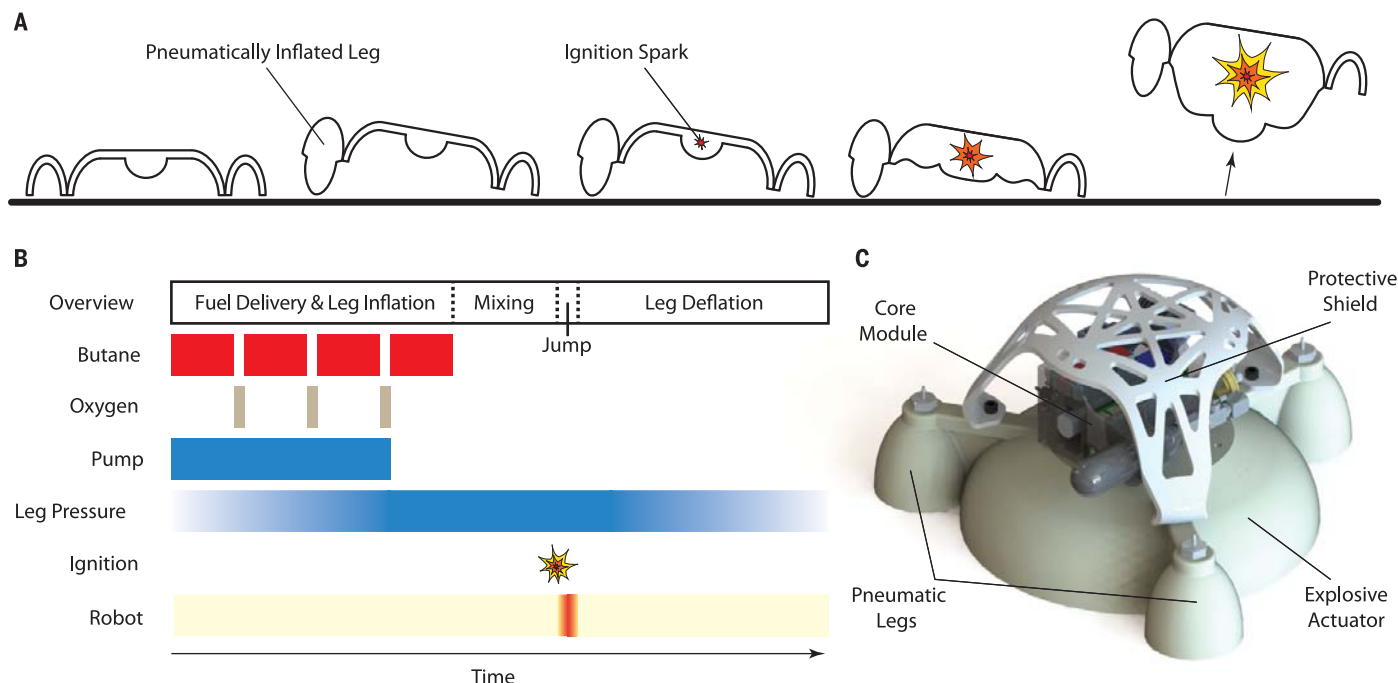


Fig. 1. Robot design and principle of operation. (A) To initiate a jump, the robot inflates a subset of its legs to tilt the body in the intended jump direction. Upon combustion, the bottom hemispheroid balloons out, pushing against the ground and propelling the robot into the air. (B) The ignition sequence consists of fuel delivery, mixing, and sparking. Butane and oxygen are alternately delivered to the combustion chamber (to promote mixing). After a short delay to

promote additional mixing of the fuels, the gaseous mixture is ignited, resulting in combustion. Leg inflation occurs concurrently with fuel delivery, and leg deflation begins shortly after landing. (C) Computer-aided design model of the entire robot, consisting of the main explosive actuator surrounded by three pneumatic legs. A rigid core module that contains power and control components sits atop the main body, protected by a semisoft shield.

The results indicate that the rigid top robot experiences a given reaction force (50 N) at a much smaller deformation than either the gradient or flexible top robots. Immediately upon impact, the rigid top robot experiences an abrupt increase in force, whereas the gradient top robot experiences a more moderate increase. The flexible top robot sees almost no increase, until the small rigid portion strikes the ground, initiating a rapid increase akin to that of the rigid top robot. Integrating the force-displacement curves (up to 50 N), we find that the rigid and flexible top robots only absorb 13 and 73% (respectively) of the impact energy that the gradient top robot absorbs. The increased energy absorbed by the gradient top robot during impact suggests that it will be most successful at distributing the impulse over a longer duration, therefore reducing peak stresses and providing the least violent landing.

By 3D-printing different test cases, we experimentally verified these simulation results. A jumping robot with a completely rigid top was able to jump 1.12 m untethered using 40 ml of butane and 120 ml of oxygen. Identical testing conditions on a gradient top robot produced a jump of 0.25 m. A flexible top robot was deemed impractical to print because of the predictions from FEA. As predicted by the simulations, the gra-

dient top robot was less efficient at jumping. However, the gradient top robot was better able to withstand the impact of landing (Fig. 3A and movie S2). In one test, the body of the rigid top robot shattered upon landing, surviving a total of just five jumps; the gradient top robot survived more than twice that number of jumps and remained operational. Other nearly identical gradient top robots survived over 100 jumps (in 81% of these tests, we removed the core module from the body and delivered the combustion products and ignition sparks through a tether to simplify testing, reducing the system mass to about 50% that of the untethered system). To provide a direct comparison in landing behavior, the gradient top robot was additionally dropped from the maximum height achieved by the rigid top robot and successfully survived 35 falls (supplementary text). The stiffness gradient provides the necessary rigidity to transfer the impulse of combustion to generate effective jumping, and the compliance of the base absorbs and dissipates the energy of the landing impact. By trading the jumping efficiency of the rigid robot for an improved ability to survive landings, the gradient top robot demonstrated a greater overall robustness.

Further testing on the gradient top robot showed high resilience and good performance (Fig. 3B and movie S2). This robot autonomously jumped

up to 0.76 m (six body heights) high and demonstrated directional jumping of up to 0.15 m (0.5 body lengths, 20% of jump height) laterally per jump (Fig. 3C and movie S2). Unlike previous combustion-powered soft jumpers that were either tethered (25) or achieved only a few untethered jumps due to inconsistent connection of electrical and mechanical components at the interface of the rigid and soft components (26), this design allowed for many successful jumps with a single soft robot (21 untethered jumps and 89 tethered jumps). Another jumper design has also shown the ability to perform multiple jumps, can operate on uneven terrain, and can even recover from landing in any orientation (27), although at the sacrifice of directional control. In our system, the high energy density of the fuels theoretically allows onboard storage of sufficient fuel for 32 consecutive jumps (supplementary text). The bodies were extremely robust, surviving dozens of jumps before they became unusable. The monolithic design has no sliding parts or traditional joints that can be fouled or obstructed by debris or rough terrain, and the nested design requires minimal deformation for actuation. As with previous jumping soft robots powered by combustion (25–27), and untethered systems exposed to direct flames (17), we did not observe significant damage to the soft (or rigid) body materials due to the brief

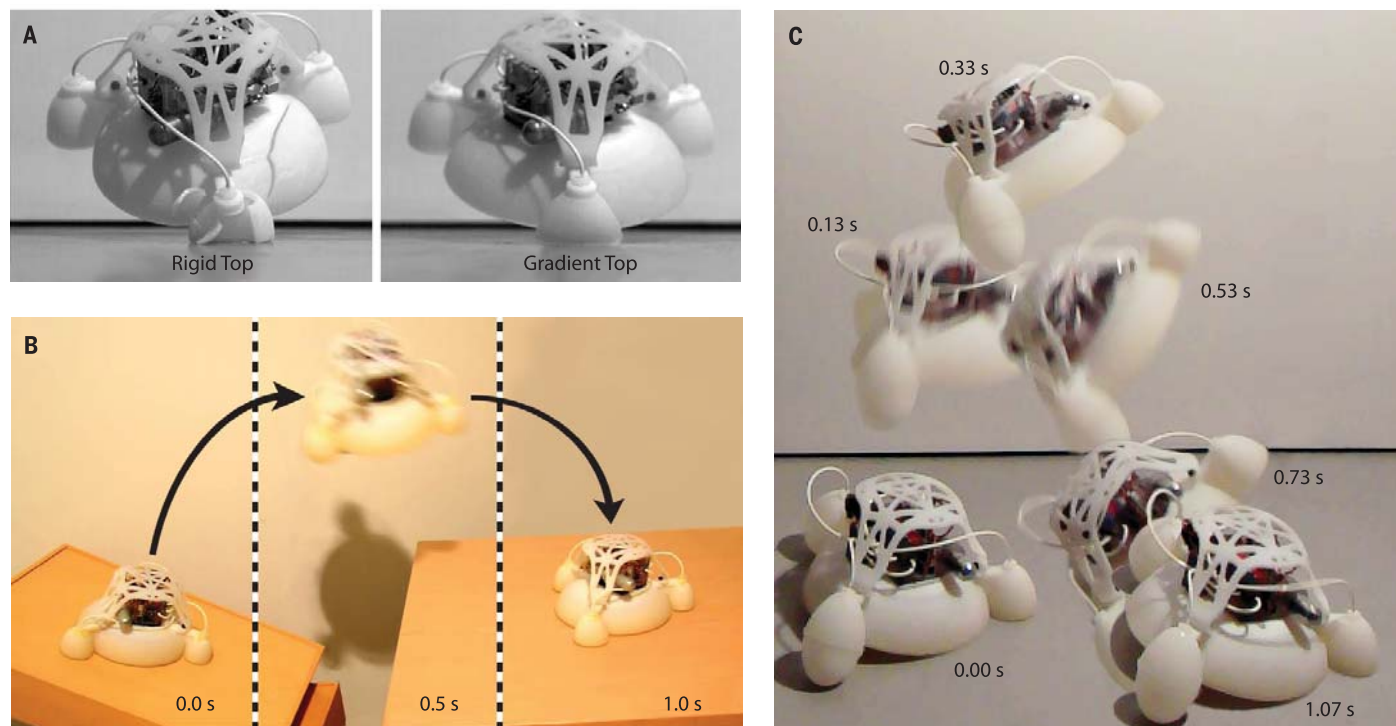


Fig. 3. Experimental testing results. (A) Frames shortly after the moment of ground contact from movie S2 (Impact Comparison). Identical testing conditions were used to analyze the difference in landing between a robot with a rigid top and one with a gradient top. Because the rigid top robot jumped higher under combustion-powered testing, the gradient top robot was dropped from the maximum height achieved by the rigid top robot for a direct comparison. (Left) The rigid top robot fractures upon impact. (Right) The gradient top robot is able to absorb the impact and survive the fall. (B) Frames from movie S2

(Jump onto Table) at various times. The robot performs a targeted jump off of an angled surface onto a table. (Left) As the robot prepares for the jump, oxygen and butane are delivered into the combustion chamber. (Middle) Upon ignition of the fuel, the robot is propelled into the air. (Right) After jumping across a gap, the robot lands on a table. (C) Frames from movie S2 (Directional Jump) at various times during a directional jump. The robot pitches backward during the jump, providing a soft landing on the inflated legs. Upon impact with the ground, the robot pitches forward and returns to its pre-jump stance.

exposure to elevated combustion temperatures and flames.

The fabrication of soft robots using multi-material 3D printing has numerous advantages over traditional molding techniques. This strategy promotes high-throughput prototyping by enabling rapid design iteration with no additional cost for increased morphological complexity. By allowing designers greater freedom, 3D printing also facilitates the implementation of good robotic design principles, such as modularity and the separation of power and control actuators. Beyond soft robotics specifically, the ability to print a single structure composed of multiple materials enables investigation into mechanically complex designs, without the drawbacks of complicated assembly or inconsistent manufacturing repeatability. One such design is a modulus gradient that eases the transition from soft to rigid components through stress reduction at the interface of materials mismatched in compliance. Although the materials available to this fabrication strategy are currently limited and perhaps best suited to the fabrication of prototype devices, future development of materials compatible with 3D printing will only enhance the relevance of this approach.

REFERENCES AND NOTES

1. D. Rus, M. T. Tolley, *Nature* **521**, 467–475 (2015).
2. D. Trivedi, C. D. Rahn, W. M. Kier, I. D. Walker, *Appl. Bionics Biomech.* **5**, 99–117 (2008).
3. R. Pfeifer, M. Lungarella, F. Iida, *Commun. ACM* **55**, 76 (2012).
4. S. Kim, C. Laschi, B. Trimmer, *Trends Biotechnol.* **31**, 287–294 (2013).
5. C. Majidi, *Soft Robotics* **1**, 5–11 (2014).
6. C. Laschi, M. Cianchetti, *Front. Bioeng. Biotechnol.* **2**, 1–5 (2014).
7. W. McMahan et al., in *Proceedings of the 2006 IEEE International Conference on Robotics and Automation*, 15 to 18 May 2006, Orlando, FL, pp. 2336–2341.
8. R. F. Shepherd et al., *Proc. Natl. Acad. Sci. U.S.A.* **108**, 20400–20403 (2011).
9. C. Laschi et al., *Adv. Robot.* **26**, 709–727 (2012).
10. H.-T. Lin, G. G. Leisk, B. Trimmer, *Bioinspir. Biomim.* **6**, 026007 (2011).
11. C. D. Onal, D. Rus, *Bioinspir. Biomim.* **8**, 026003 (2013).
12. A. D. Marchese, C. D. Onal, D. Rus, *Soft Robotics* **1**, 75–87 (2014).
13. R. Pfeifer, M. Lungarella, F. Iida, *Science* **318**, 1088–1093 (2007).
14. K. Suzumori, S. Iikura, H. Tanaka, *Control Syst. IEEE* **12**, 21–27 (1992).
15. Y.-L. Park et al., *Bioinspir. Biomim.* **9**, 016007 (2014).
16. P. Polygerinos, Z. Wang, K. C. Galloway, R. J. Wood, C. J. Walsh, *Robot. Auton. Syst.*; available at www.sciencedirect.com/science/article/pii/S0921889014001729.
17. M. T. Tolley et al., *Soft Robotics* **1**, 213–223 (2014).
18. H. Lipson, *Soft Robotics* **1**, 21–27 (2014).
19. K.-J. Cho et al., *Int. J. Precision Eng. Manuf.* **10**, 171–181 (2009).
20. F. Ilievski, A. D. Mazzeo, R. F. Shepherd, X. Chen, G. M. Whitesides, *Angew. Chem.* **123**, 1930–1935 (2011).
21. E. Steltz, A. Mozeika, N. Rodenberg, E. Brown, H. M. Jaeger, in *Proceedings of the 2009 IEEE/RSJ International Conference on Intelligent Robots and Systems*, 10 to 15 October 2009, St. Louis, MO, pp. 5672–5677.
22. T. J. Roberts, E. Azizi, *J. Exp. Biol.* **214**, 353–361 (2011).
23. A. Miserez, T. Schneberk, C. Sun, F. W. Zok, J. H. Waite, *Science* **319**, 1816–1819 (2008).
24. Materials and methods are available as supplementary materials on Science Online.
25. R. F. Shepherd et al., *Angew. Chem.* **125**, 2964–2968 (2013).
26. M. T. Tolley et al., in *Proceedings of the 2014 IEEE/RSJ International Conference on Intelligent Robots and Systems*, 14 to 18 September 2014, Chicago, IL, pp. 561–566.
27. M. Loepef, C. M. Schumacher, U. B. Lustenberger, W. J. Stark, *Soft Robotics* **2**, 33–41 (2015).

ACKNOWLEDGMENTS

This material is based on work supported by NSF under award number DMR-1420570; the Wyss Institute for Biologically Inspired Research; and an Army Research Office, National Defense Science and Engineering Graduate (NDESG) fellowship. Any opinions,

findings, conclusions, or recommendations expressed in this material are those of the authors and do not necessarily reflect those of the funding organizations.

SUPPLEMENTARY MATERIALS

www.sciencemag.org/content/349/6244/161/suppl/DC1

Materials and Methods
Supplementary Text
Figs. S1 and S2
Table S1
References (28, 29)
Movies S1 and S2

27 February 2015; accepted 11 June 2015
10.1126/science.aab0129

APPLIED PHYSICS

Mid-infrared plasmonic biosensing with graphene

Daniel Rodrigo,¹ Odeta Limaj,¹ Davide Janner,² Dordaneh Etezadi,¹ F. Javier García de Abajo,^{2,3} Valerio Pruneri,^{2,3} Hatice Altug^{1*}

Infrared spectroscopy is the technique of choice for chemical identification of biomolecules through their vibrational fingerprints. However, infrared light interacts poorly with nanometric-size molecules. We exploit the unique electro-optical properties of graphene to demonstrate a high-sensitivity tunable plasmonic biosensor for chemically specific label-free detection of protein monolayers. The plasmon resonance of nanostructured graphene is dynamically tuned to selectively probe the protein at different frequencies and extract its complex refractive index. Additionally, the extreme spatial light confinement in graphene—up to two orders of magnitude higher than in metals—produces an unprecedentedly high overlap with nanometric biomolecules, enabling superior sensitivity in the detection of their refractive index and vibrational fingerprints. The combination of tunable spectral selectivity and enhanced sensitivity of graphene opens exciting prospects for biosensing.

Graphene has the potential to reshape the landscape of photonics and optoelectronics owing to its exceptional optical and electrical properties (*1–3*). In particular, its infrared (IR) response is characterized by long-lived collective electron oscillations (plasmons) that can be dynamically tuned by electrostatic gating, in contrast to conventional plasmonic materials such as noble metals (*4–10*). Furthermore, the electromagnetic fields of graphene IR plasmons display unprecedented spatial confinement, making them extremely attractive for enhanced light-matter interactions and integrated mid-IR photonics (*11–14*). Specifically, biosensing is an area in which graphene tunability and IR light localization offer great opportunities.

The mid-IR range is particularly well suited for biosensing, as it encompasses the molecular vibrations that uniquely identify the biochemical building blocks of life, such as proteins, lipids, and DNA (*15*). IR absorption spectroscopy is a powerful technique that provides exquisite bio-

chemical information in a nondestructive label-free fashion by accessing these vibrational fingerprints. Nevertheless, vibrational absorption signals are prohibitively weak because of the large mismatch between mid-IR wavelengths (2 to 6 μm) and biomolecular dimensions (<10 nm). To overcome this limitation, high sensitivity can be achieved by exploiting the strong optical near fields in the vicinity of resonant metallic nanostructures (*16–18*); however, this comes at the expense of a reduced spectral bandwidth and is ultimately limited by the relatively poor field confinement of metals in the mid-IR (*19*).

Here, we report a graphene-based tunable mid-IR biosensor and demonstrate its potential for quantitative protein detection and chemical-specific molecular identification. Our device (Fig. 1A) consists of a graphene layer synthesized by chemical vapor deposition and transferred to a 280-nm-thick native silica oxide of a silicon substrate. Graphene nanoribbon arrays (width $W = 20$ to 60 nm and period $P \approx 2W$) are then patterned using electron beam lithography and oxygen plasma etching (*20*). A scanning electron microscope image and an atomic force microscope profile for typical samples are shown in Fig. 1, B and C. We apply an electrostatic field across the SiO_2 layer through a bias voltage (V_g)

¹Institute of BioEngineering, École Polytechnique Fédérale de Lausanne, CH-1015 Lausanne, Switzerland. ²Institut de Ciències Fotòniques, Mediterranean Technology Park, 08860 Castelldefels (Barcelona), Spain. ³Institució Catalana de Recerca i Estudis Avançats, 08010 Barcelona, Spain.

*Corresponding author. E-mail: hatice.altug@epfl.ch

This copy is for your personal, non-commercial use only.

If you wish to distribute this article to others, you can order high-quality copies for your colleagues, clients, or customers by [clicking here](#).

Permission to republish or repurpose articles or portions of articles can be obtained by following the guidelines [here](#).

The following resources related to this article are available online at www.sciencemag.org (this information is current as of August 27, 2015):

Updated information and services, including high-resolution figures, can be found in the online version of this article at:

<http://www.sciencemag.org/content/349/6244/161.full.html>

Supporting Online Material can be found at:

<http://www.sciencemag.org/content/suppl/2015/07/08/349.6244.161.DC1.html>

This article **cites 23 articles**, 4 of which can be accessed free:

<http://www.sciencemag.org/content/349/6244/161.full.html#ref-list-1>

This article has been **cited by** 1 articles hosted by HighWire Press; see:

<http://www.sciencemag.org/content/349/6244/161.full.html#related-urls>

This article appears in the following **subject collections**:

Engineering

<http://www.sciencemag.org/cgi/collection/engineering>